Dirac imprints on the *g*-factor anisotropy in graphene

M. Prada,[1,*] L. Tiemann,[2,*] J. Sichau,[2,*] and R. H. Blick[2,3]
[1]*HARBOR, Universität Hamburg, Luruper Chaussee 149, 22761 Hamburg, Germany*
[2]*CHyN, Universität Hamburg, Luruper Chaussee 149, 22761 Hamburg, Germany*
[3]*Materials Science and Engineering, University of Wisconsin–Madison, 1509 University Avenue, Madison, Wisconsin 53706, USA*

(Received 11 December 2020; revised 10 May 2021; accepted 29 June 2021; published 2 August 2021)

Dirac electrons in graphene are to lowest order spin 1/2 particles, owing to the orbital symmetries at the Fermi level. However, anisotropic corrections in the *g* factor appear due to the intricate spin-valley-orbit coupling of chiral electrons. We resolve experimentally the *g* factor along the three orthogonal directions in a large-scale graphene sample. We employ a Hall bar structure with an external magnetic field of arbitrary direction, and extract the effective *g* tensor via resistively detected electron spin resonance. We employ a theoretical perturbative approach to identify the intrinsic and extrinsic spin orbit coupling and obtain a fundamental parameter inherent to the atomic structure of ^{12}C, commonly used in *ab initio* models.

DOI: 10.1103/PhysRevB.104.075401

I. INTRODUCTION

One of the great triumphs of the Dirac relativistic theory for the electron was the prediction of the *g* factor with the value $g_0 \simeq 2$ [1]. As a major departure from previous quantum theories, Dirac's equation describes indeed spin 1/2 particles with four-component spinors or bispinors, allowing one to introduce the concepts of chirality and helicity. Chirality is an inherent property of the particle, whereas helicity depends on its momentum: namely, it is positive (negative) when the momentum aligns (anti)parallel to the spin. In the massless limit, both qualities are related [2]: positive chirality corresponds to positive helicity and vice versa.

The linear dispersion at the Fermi level of graphene is cognate with the Dirac cones of the massless relativistic particles [3], motivating extensive research towards the parallelism with relativistic quantum mechanics in a solid-state material [4–9]. The inherent chirality of the Dirac carriers leads to a topologically nontrivial band structure [10–13]. Although the carriers are, to lowest order, spin 1/2 particles, their chirality induces a coupling of spin, valley, and orbital degrees of freedom [14]. Here, we address this particular coupling that appears as a measurable *g*-factor anisotropy.

From a theoretical perspective, the Zeeman Hamiltonian that describes the interaction with an applied field is given by the sum of the contributions of the orbital and spin angular momenta, *L* and *S*, respectively [15]:

$$\hat{H}_Z = \mu_B \vec{B}(\hat{\vec{L}} + g_0 \hat{\vec{S}}),$$

with g_0 representing the pure *g* factor, μ_B the Bohr magneton, and $\vec{B}$ an external magnetic field. On the other hand, the *effective* spin model, commonly employed experimentally to describe the Zeeman energy, includes an *effective* *g* tensor and *fictitious* spin operators [16–18],

$$\hat{H}_{\text{eff}} = \mu_B \vec{B} \tilde{\boldsymbol{g}} \hat{\vec{S}}.$$

$\tilde{\boldsymbol{g}}$ must be constructed such that the energies obtained with the effective spin Hamiltonian capture the corrections due to the internal molecular orbital angular momentum. In electron-spin resonance (ESR) experiments, this internal structure modifies the strength of an external field necessary to meet the resonant condition [19]:

$$h\nu = \mu_B \langle \vec{B}(\hat{\vec{L}} + g_0 \hat{\vec{S}}) \rangle = \mu_B \langle \vec{B} \tilde{\boldsymbol{g}} \hat{\vec{S}} \rangle, \tag{1}$$

where $\tilde{\boldsymbol{g}}$ is a tensor that contains the effective (or experimental) *g* factors measured with the field along the corresponding directions and $\langle \cdot \rangle$ indicates the expectation value. Since the *g* tensor is diagonal along the crystallographic directions, the angular dependence for the general rhombic symmetry can be expressed in terms of g_{xx}, g_{yy}, and g_{zz} [17]:

$$g(\theta, \varphi) = \sqrt{g_{zz}^2 \cos^2\theta + g_{yy}^2 \sin^2\theta \sin^2\varphi + g_{xx}^2 \sin^2\theta \cos^2\varphi}, \tag{2}$$

for an arbitrary magnetic field with axial and azimuthal angles θ, φ. In this paper we resolve experimentally the effective *g* factor along the three main directions in a mesoscopic graphene sample, $g_{\alpha\alpha} = g_0 + \Delta g_{\alpha\alpha}$, whereas the corresponding theoretical correction is evaluated perturbatively via the expectation value of the angular momentum, $\Delta g_{\alpha\alpha} = \langle \hat{L}_\alpha \rangle$, $\alpha = x, y, z$. We employ a microscopic perturbative model to obtain $\Delta g_{\alpha\alpha}$ in terms of atomic parameters [14]. We then compare these theoretical values to our experimentally obtained *g* factors and extract the atomic spin-orbit coupling (SOC) corrections.

II. THEORETICAL BACKGROUND

It is commonly accepted that near the Dirac points (DPs) the eigenstates are described by π orbitals near the Fermi

*These authors contributed equally to this work.

edge [20]. The conduction and valence bands, to lowest order, are linear in momentum, with the corresponding *chiral* states given in terms of the main (p_z-orbital) contribution at sublattices A and B [20,21]:

$$|\psi_{\pm}^{(0)}\rangle \simeq c_A|p_z^A\rangle + c_B|p_z^B\rangle,$$
$$\frac{c_B}{c_A} = \pm e^{i\varphi_q\tau}, \tag{3}$$
$$\varphi_q = \arctan\frac{q_y}{q_x},$$

where the sign $\pm$ labels the conduction band (CB) and valence band (VB), respectively. These DPs are the celebrated K and K' points, which are assigned the valley index, $\tau = 1$ and -1, respectively, and $\vec{q} = (q_x, q_y)$ is the small vector off the nearest DP. The chirality-preserving Kane-Mele intrinsic SOC term [10], $\hat{H}_{\rm KM} = \tau\lambda_{\rm I}\hat{s}_z\hat{\sigma}_z$, with $\hat{s}_z$, $\hat{\sigma}_z$ being the Pauli matrices representing the electron spin and sublattice spin, respectively, leads to the spin Hall effect and a measurable intrinsic SOC gap $\Delta_{\rm I} = 2\lambda_{\rm I}$ [12,22,23]. As we will show, the intrinsic SOC leads as well to *chiral* spin-valley orbit coupling and additional corrections to the measured g factor. To lowest order, the quasiparticle eigenenergies are given by

$$\varepsilon_{\pm} = \pm\sqrt{(\hbar v_F q)^2 + \lambda_{\rm I}^2}. \tag{4}$$

with v_F being the Fermi velocity. The axial symmetry of the p_z orbitals involves $\langle\hat{L}_\alpha\rangle = 0$, and hence, the g factor at lowest order is that of free electrons. Dominant corrections to the g factor are due to (i) band hybridization, (ii) atomic SOC, (iii) Bychkov-Rashba effect, and (iv) structural SOC, which we consider in the following.

As pointed out by McClure *et al.* [24], the π bands are p_z orbitals hybridized with d_{xz} and d_{yz} orbitals of the nearest neighbor (NN). Owing to the large energy difference, the p_z contribution is dominant near the Fermi energy. Using that, e.g., the hopping $p_z^A \to d_{xz}^B$ is given by $V_{pd\pi}\sum_i m_i \exp i\vec{k}\vec{\delta}_i$, with the vectors connecting NN given by $\vec{\delta}_i = (l_i, m_i)$, with $\vec{\delta}_{1,2} = (\pm\sqrt{3}, -1)/2$ and $\vec{\delta}_3 = (0, 1)$, and $V_{pd\pi}$ is the relevant p-d coupling. Near the DP, $\vec{K} = (0, 4\pi\tau/(3a\sqrt{3}))$, one obtains $V_{p_z^A\to d_{xz}^B} = 3V_{pd\pi}/2$ and $V_{p_z^A\to d_{yz}^B} = -3iV_{pd\pi}/2$. We then obtain perturbatively the d-band contribution [25–27],

$$|\psi_d^{(1)}\rangle = \sum_{i,\alpha=A,B}\frac{\langle d_i^\alpha|\hat{V}_{\rm h}|\psi^{(0)}\rangle}{\varepsilon_{pd}}$$
$$= \frac{3i\tau V_{pd\pi}}{\sqrt{2}\varepsilon_{pd}}[c_A|2,\tau\rangle^B + c_B|2,-\tau\rangle^A], \tag{5}$$

where ε_{pd} is the energetic difference between the d and p orbitals. Here, we have expressed the d orbitals in the angular momentum representation, $|l, m_l\rangle$, with the definitions

$$|1,\pm1\rangle = \frac{1}{\sqrt{2}}(|p_x\rangle \mp i|p_y\rangle),$$
$$|2,\pm1\rangle = \frac{1}{\sqrt{2}}(|d_{xz}\rangle \mp i|d_{yz}\rangle).$$

It is worth noting in Eq. (5) that m_l relates to the valley index, τ, commonly termed as *valley-orbit* coupling. This is connected to the chirality of the Dirac electrons: in one sublattice, the p_z electrons couple to those of d-orbital with $m_l = 1$ ($m_l = -1$) in valley K (K'), and the converse occurs for the other sublattice [14]. As we will see below, this has important consequences for the g-factor corrections (see diagram of Fig. 1).

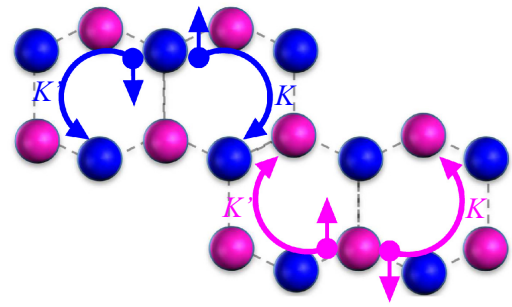

FIG. 1. Illustration of the spin-valley-orbit coupling of Dirac carriers in the top valence band. Spin "down" carriers couple to counterclockwise ($m_l = 1$) rotating orbitals, whereas spin "up" carriers couple to clockwise ($m_l = -1$) rotating orbitals.

On the other hand, the σ band is constituted of s and $p_{x,y}$ of the NN [28]. The π bands described by Eqs. (3) and (5) can mix with the σ bands either intrinsically via atomic spin-orbit interaction or extrinsically, via structural SOC or Bychkov-Rashba effect. The latter emerges as the horizontal mirror symmetry breaks and is linear in (uniaxial) electric field [26,29–31], leading to an atomic dipole moment, commonly termed the Stark effect. Microscopically, the induced dipole results in a nonzero intra-atomic coupling between the p_z and s orbitals. The structural SOC is related to a horizontal plane mirror asymmetry (PIA) [32–35] originated by ripples, defects, or adsorbates, coupling p_z and $p_{x,y}$ orbitals.

The σ-band mixing near the Fermi energy is expected to be smaller than the d-band contribution, since the atomic SOC parameter and the Stark parameter, $\lambda_z = eE\langle s|\hat{z}|p_z\rangle$ are small compared to the p-d coupling, $\lambda_{\rm soc}^p, \lambda_a, \lambda_z \ll V_{pd\pi}$. We thus consider the σ-band mixing perturbatively, $\hat{V} = \hat{V}_{\rm soc} + \hat{V}_{\rm PIA} + \hat{V}_{\rm EF}$, with

$$\hat{V} = i\epsilon_{ijk}\hat{s}_k\left(\lambda_{\rm soc}^p|p_i^\alpha\rangle\langle p_j^\alpha| + \lambda_{\rm a}|p_i^\alpha\rangle\langle p_j^{\overline{\alpha}}| + \lambda_z|s_i^\alpha\rangle\langle p_z^\alpha|\right) + {\rm H.c.}, \tag{6}$$

where we have included the atomic p-orbital coupling $\lambda_{\rm soc}^p$ and structural SOC in λ_a and the Einstein summation convention is assumed.

The projection over the orbital eigenstates yielding finite angular momentum contributions are [14]

$$\hat{\mathcal{P}}|\psi_\sigma^{(1)}\rangle = \left(\tau\alpha_I^\sigma c_A - is_z\alpha_E^\sigma c_B\right)|1,-\tau\rangle^A$$
$$-\left(\tau\alpha_I^\sigma c_B - is_z\alpha_E^\sigma c_A\right)|1,\ \tau\rangle^B, \tag{7}$$

where $\hat{\mathcal{P}} = |1,1\rangle\langle1,1| + |1,-1\rangle\langle1,-1|$ and α_I^σ, α_E^σ are the σ-band intrinsic and extrinsic SOC coefficients (see the Appendix):

$$\alpha_I^\sigma = \lambda_{\rm soc}^p\left(\frac{\sin^2\gamma}{2\varepsilon_\sigma^+} + \frac{\cos^2\gamma}{2\varepsilon_\sigma^-}\right), \quad \alpha_E^\sigma = \alpha_{\rm BR} + \alpha_{\rm PIA}$$

with $\tan\gamma = 3\sqrt{2}V_{sp\sigma}/2\varepsilon_\sigma^+$, $V_{sp\sigma}$ being the σ coupling of the p and s orbitals and $\varepsilon_\sigma^\pm = \varepsilon_s \pm \sqrt{\varepsilon_s^2 + 2(3V_{sp\sigma})^2}/2$.

Finally, $\alpha_{\rm BR}$ and $\alpha_{\rm PIA}$ account for the Bychkov-Rashba and the sublattice asymmetry SOC, respectively.

Equations (5) and (7) yield three different second order contributions for $\langle \hat{L}_z \rangle$, that is, $\Delta g_{zz} = \sum_i \langle \psi_i^{(1)} | \hat{L}_z | \psi_i^{(1)} \rangle$, giving

$$\Delta g_{zz} \simeq \tau \sigma_z^0 \left(\left| \frac{\lambda_I}{\lambda_{\rm soc}^d} \right| - \left(\alpha_I^\sigma\right)^2 + \left(\alpha_E^\sigma\right)^2 \right), \tag{8}$$

where we have defined $\sigma_z^0 \equiv \langle \psi_\pm^{(0)} | \hat{\sigma}_z | \psi_\pm^{(0)} \rangle = |c_A|^2 - |c_B|^2$, and we have used the result of Konschuh *et al.* [26], $\lambda_I = 9V_{pd\pi}^2 \lambda_{\rm soc}^d / (2\epsilon_{pd}^2)$, with $\lambda_{\rm soc}^d$ being the atomic SOC for the d orbitals. We note that all three terms are proportional to $\tau \langle \sigma_z \rangle$, due to the valley-orbit coupling, and the first term is dominant, as we will see.

Figure 1 illustrates the underlying nature of the spin-valley-orbit coupling for the lowest bands given in Eq. (4). The highest populated state is characterized by $\tau s_z \sigma_z = -1$. For sublattice B (blue, $\sigma_z = -1$), the state has spin "up" in the K-valley, and it couples to an anti-clockwise rotating d orbital, whereas the spin "down" in the K' valley couples to the clockwise rotating d orbital. The converse occurs for sublattice A (magenta, $\sigma_z = 1$), where the spin "up" ("down") is in the K' (K) valley, but it couples to the $m_l = -1$ ($m_l = 1$) d orbital.

Hence, in the presence of spin-valley-orbit coupling, the Dirac carrier's spin direction opposes that of the m_l quantum number of the coupled d orbital, reducing the effective g factor at leading order.

We now consider the in-plane corrections, $\langle L_x \rangle$ and $\langle L_y \rangle$, with $\Delta g_{\alpha\alpha} = 2\Re \langle \psi_\pm^{(0)} | \hat{L}_\alpha | \psi_\sigma^{(1)} \rangle$. We choose the $\hat{x}$ axis to be parallel to a zig-zag direction. The theoretical model assumes a well-defined crystalline zig-zag direction, which can be generalized as the transport direction in the polycrystalline, continuum limit. Within the basis spanned by $m_l = \{1, 0, -1\}$, we define

$$\hat{L}_+ = \begin{pmatrix} 0 & \sqrt{2} & 0 \\ 0 & 0 & \sqrt{2} \\ 0 & 0 & 0 \end{pmatrix}, \quad \hat{L}_- = \begin{pmatrix} 0 & 0 & 0 \\ \sqrt{2} & 0 & 0 \\ 0 & \sqrt{2} & 0 \end{pmatrix},$$
$$\hat{L}_z = \begin{pmatrix} 1 & 0 & 0 \\ 0 & 0 & 0 \\ 0 & 0 & -1 \end{pmatrix}, \quad \hat{L}_\pm = \frac{1}{2}(\hat{L}_x \pm i\hat{L}_y). \tag{9}$$

Using Eq. (7) and $\sqrt{2}\hat{L}_x |1, \pm\tau\rangle^\alpha = |p_z^\alpha\rangle$, we obtain first order corrections:

$$\Delta g_{xx} = \pm 2\sqrt{2}\left(\alpha_I^\sigma \tau \sigma_z^0 + \alpha_E^\sigma s_z \tau \sin\varphi_q\right),$$
$$\Delta g_{yy} = \mp 2\sqrt{2}\alpha_E^\sigma s_z \tau \cos\varphi_q. \tag{10}$$

The intrinsic contribution results in a (dominant) negative correction for the highest populated band, whereas the sign of the extrinsic one depends on the electric field direction. In a single-particle theoretical picture, *all* corrections would vanish, as $\langle \tau \hat{\sigma}_z \rangle$ averages out to zero. However, under real experimental conditions and in a macroscopic graphene sample with a spin imbalance $n_\uparrow - n_\downarrow \neq 0$, the problem becomes many body and corrections to the g factor emerge.

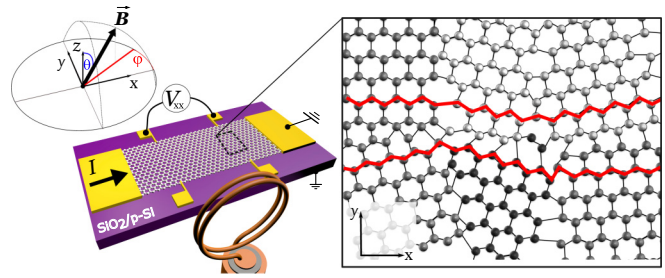

FIG. 2. Schematic setup of our ESR measurements. The external magnetic field $|B| \lesssim 1$ T can freely rotate, while a Hertzian loop antenna induces an AC field. A constant current flows along the x direction, and the longitudinal voltage V_{xx} is measured. The graphene layer rests on 300 nm SiO_2 on top of a p-Si substrate that is grounded. The blow-up on the right-hand side illustrates the granular nature of the CVD graphene. The polycrystallinity retains zig-zag directions (red bold lines) parallel to the transport current.

III. EXPERIMENTAL RESULTS

We experimentally scrutinize the spin-valley-orbit coupling and the validity of our model by studying the g tensor in a large-scale (1960 μm × 66 μm) graphene Hall bar on SiO_2. The device fabrication processes of the graphene that was synthesized by chemical vapor deposition are described by Lyon *et al.* [36]. We employed low temperature (1.4 K) resistively detected electron-spin resonance (RD-ESR) [12,37,38], a spin-selective probing technique that couples carriers of opposite spin by microwave excitation, and detects the response resistively. The large dimension of our device ensures the continuum limit with a well-defined bulk gap and chirality for the charge carriers [10]. We assume, for simplicity, that the polycrystalline nature of the sample retains the theorized zig-zag directions parallel to the transport directions, as illustrated in Fig. 2. Polycrystallinity also induces disorder, which broadens the resonant signal and facilitates the resistive detection.

The microwave excitation field is generated by a Hertzian loop antenna adjacent to the sample [see Fig. 2]. A constant low frequency current $I = 1$nA is passed through the sample along x direction, which we can relate to the *propagating* zig-zag direction (blow-up in Fig. 2), while a standard lock-in technique probes the resulting longitudinal resistance, $R_{xx} = V_{xx}/I$, as a function of the magnetic field $\vec{B}$. The magnetic field vector $\vec{B}$ can freely rotate with respect to the sample plane. Hence, we use spherical coordinates to denote the orientation of $\vec{B}$, with θ as the out-of-plane angle and φ for in-plane rotations. All measurement are performed without the application of a gate voltage (substrate grounded), corresponding to an intrinsic density of $n \approx 6 \times 10^{11}$ cm^{-2}.

Whenever the microwave frequency ν matches the resonant condition of Eq. (1), the increased band population reduces $R_{xx,\nu}$. We can resolve these resonances as peaks in the microwave-induced differential resistance, $\Delta R_{xx}(\nu) = R_{xx,\rm dark} - R_{xx,\nu}$.

Figure 3 shows the electron spin resonances for different values of $|\vec{B}|$ under constant angle θ in the x-z plane. Each data point is the result of a Gaussian fit to the resonance curves $\Delta R_{xx}(\nu)$ (not shown). The data points follow a linear dispersion that reflects the magnetic field dependence of the

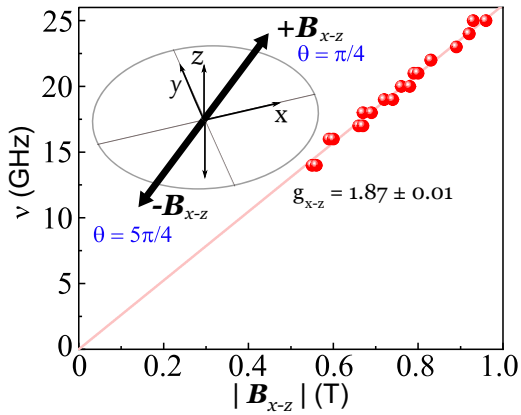

FIG. 3. Resonance frequency as a function of field strength $|\vec{B}|$ at constant θ in the x-z plane. The data are taken at $T = 1.4$ K, with a microwave radiation power of 21 dBm. The g factor is given by the slope of the linear fit, $g_{xz} = 1.87 \pm 0.01$.

Zeeman energy. Its slope thus represents the *effective* g factor of the Dirac electrons for the magnetic field under θ.

The procedure is repeated for $\vec{B}$ pointing in different directions, i.e., for various θ and φ, allowing us to resolve the anisotropic g factor as defined in Eq. (2). Figure 4 is an angle-resolved study of the effective g factor within the planes marked schematically inside each graph. In Fig. 4(a) we explore the y-z plane, where a sinusoidal dependence of the g factor on the axial angle θ is apparent. When the external field is oriented perpendicular to the sample plane ($\theta = 0$) we obtain $g_{zz} = 1.95 \pm 0.02$ [12], whereas for $\theta = 90^\circ$ we obtain $g_{yy} = 2.03 \pm 0.02$. Figure 4(b) shows a rotation of θ in the $y = 0$ plane. Here, the effective g factor is smallest when $\vec{B}$ is collinear to the current direction and becomes $g_{xx} = 1.81 \pm 0.02$. This is further supported by the in-plane anisotropy (at fixed $\theta = \pi/2$) shown in Fig. 4(c), and is consistent with our assumption of a predominant zig-zag transport direction. We attribute the asymmetry to the current-induced Rashba effect [39] and to the polycrystalline structure of the graphene, where the current direction is defined only locally, as illustrated in Fig. 2. The largest correction is thus obtained for $\Delta g_{xx} = -0.19 \pm 0.01$, consistent with the first order intrinsic SOC, and the smallest correction is $\Delta g_{yy} = 0.03 \pm 0.01$, consistent with a small extrinsic SOC in the absence of gating. Finally, $\Delta g_{zz} = -0.05 \pm 0.01$, corresponding to a second order correction. Table I summarizes the experimentally extracted elements of the g tensor and the g-factor anisotropy.

TABLE I. Experimentally determined effective g factors for the three orthogonal directions obtained at 1.4 K.

g_x	$g_{x\text{-}y}$	g_y	$g_{y\text{-}z}$	g_z	$g_{x\text{-}z}$	Error
1.81	1.91	2.03	1.99	1.95	1.87	0.01

We can extract atomic SOC parameters that lead to the observed g-factor corrections. For the in-plane corrections, using (10) with $\varphi_q = 0$, we obtain $\alpha_E^\sigma \simeq (0.01 \pm 0.03)$. We also obtain $\alpha_I^\sigma \simeq (0.067 \pm 0.003)$, giving an upper limit for $\lambda_{\rm soc}^p < 0.05\varepsilon_s$, consistent with the theoretical value [26–28,30,31,40,41].

For the axial correction, using $\lambda_I \simeq 21\ \mu$eV [12] in Eq. (8) we obtain SOC parameter for d orbitals, $\lambda_{\rm soc}^d$,

$$\lambda_{\rm soc}^d \simeq (0.31 \pm 0.09)\ \text{meV},$$

which compares quite well with the DFT obtained value of 0.8 meV [26]. As pointed out by Konschuh *et al.*, unlike in the $\lambda_{\rm soc}^p$ case, there is no possible fitting of the energy spectrum to obtain numerically this value, since the needed high-energy states in the conduction bands cannot be identified. We stress that this value is *intrinsic*: it is the atomic spin-orbit coupling not only for the special case of graphene, but for all ^{12}C atoms.

IV. CONCLUSIONS

In summary, we experimentally resolved the g-factor anisotropy in graphene using an angle-dependent ESR method. The chiral nature of the Dirac electrons in graphene entails corrections to the g factor that originate from a peculiar spin-valley orbit coupling. Along the transport direction, we observe a negative first order correction, owing to the intrinsic, chiral SOC with the propagating p_x orbital. We extract an intrinsic coupling of $\alpha_I^\sigma \simeq 0.067 \pm 0.003$. Along the y direction, the sign and magnitude of the g-factor correction reflect an extrinsic SOC, consistent with the absence of inversion symmetry. We extract an extrinsic coupling of $\alpha_E^\sigma \simeq 0.001 \pm$

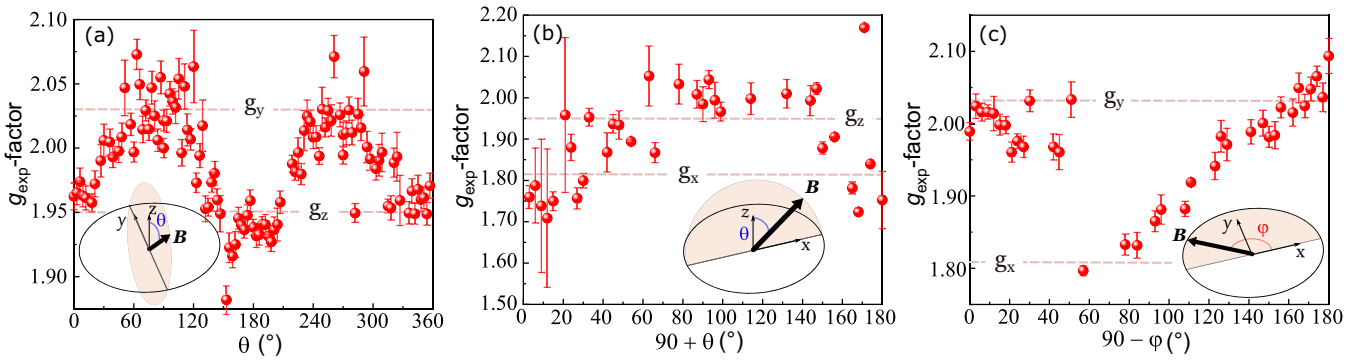

FIG. 4. Angular dependence of the g factor: (a) g factor for a rotation of θ in the y-z plane and (b) for a rotation of θ in the x-z plane and (c) for a rotation of φ in the x-y plane. Along the in-plane, we extract $\Delta g_{xx} = -0.19 \pm 0.01$ and $\Delta g_{yy} = 0.03 \pm 0.01$, whereas $\Delta g_{zz} = -0.05 \pm 0.01$.

0.003. In combination with the axial correction, we were able to extract intrinsic SOC parameter $\lambda_{\rm soc}^{d} = 0.31 \pm 0.09$ meV.

ACKNOWLEDGMENTS

We acknowledge support by the Bundesminsterium für Forschung und Technologie (BMBF) through the "Forschungslabor Mikroelectronik Deutschland (ForLab)." We thank Hans-Peter Oepen and T. Schmirander for fruitful discussions. All experiments were performed with NANOMEAS [42].

APPENDIX: σ BAND MIXING VIA SOC

The σ bands near the DPs can be expressed within a reduced Hilbert space spanned by $\{s^{\alpha}, p_x^{\beta}, p_y^{\eta}\}$ [14,30]:

$$\begin{aligned}
|\psi_{AB}^{+}\rangle &= i\tau\cos\gamma|s^{A}\rangle + \sin\gamma|1,\tau\rangle^{B},\\
|\psi_{BA}^{+}\rangle &= i\tau\cos\gamma|s^{B}\rangle + \sin\gamma|1,-\tau\rangle^{A}\\
|\psi_{AB}^{-}\rangle &= -i\tau\sin\gamma|s^{A}\rangle + \cos\gamma|1,\tau\rangle^{B},\\
|\psi_{BA}^{-}\rangle &= -i\tau\sin\gamma|s^{B}\rangle + \cos\gamma|1,-\tau\rangle^{A},
\end{aligned} \tag{A1}$$

where the corresponding energies, to lowest order, can be expressed in terms of the hopping $V_{sp\sigma}$ and the s orbital energy, ε_s, namely:

$$\varepsilon_{\sigma}^{\pm} = \frac{\varepsilon_s}{2} \pm \sqrt{\frac{\varepsilon_s^2}{4} + \frac{9V_{sp\sigma}^2}{2}},$$

and we have defined $\tan\gamma = 3V_{sp\sigma}/\sqrt{2}\varepsilon_{\sigma}^{+}$.

We consider the mixing of the p_z and the σ bands (A1) due to SOC. Using the first term of the expression (6) we obtain the action of $V_{\rm soc}$ over a general p_z orbital with spin $\hat{s}_z|s_z\rangle = (s_z/2)|s_z\rangle$, with $s_z = \pm 1$:

$$\begin{aligned}
\hat{V}_{\rm soc}\left|p_z^{\alpha}\right\rangle \otimes |s_z\rangle &= \frac{i\lambda_{\rm soc}^{p}}{2}(|p_y\rangle^{\alpha} - is_z|p_y\rangle^{\alpha}) \otimes |-s_z\rangle\\
&= \frac{s_z\lambda_{\rm soc}^{p}}{\sqrt{2}}|1,-s_z\rangle^{\alpha} \otimes |-s_z\rangle.
\end{aligned}$$

Assuming the expectation value for the spin components $\langle s_{x,y}\rangle = 1/2$, we then get the first order correction to the π bands of Eq. (3), were the orbital part gives

$$\begin{aligned}
\left|\psi_{\rm at}^{(1)}\right\rangle &= \sum_{s,\alpha\neq\beta}\frac{\left\langle\psi_{\alpha\beta}^{s}\middle|\hat{V}_{\rm soc}\middle|\psi^{(0)}\right\rangle}{\varepsilon_{\sigma}^{s}}\left|\psi_{\alpha\beta}^{s}\right\rangle = \frac{s_z\lambda_{\rm soc}^{p}}{2}\left\{\frac{\cos\gamma}{\varepsilon_{\sigma}^{-}}\left[c_A\delta_{s_z,-\tau}|\psi_{BA}^{-}\rangle + c_B\delta_{s_z,\tau}|\psi_{AB}^{-}\rangle\right] + \frac{\sin\gamma}{\varepsilon_{\sigma}^{+}}\left[c_A\delta_{s_z,-\tau}|\psi_{BA}^{+}\rangle + c_B\delta_{s_z,\tau}|\psi_{AB}^{+}\rangle\right]\right\}\\
&= \tau\frac{\lambda_{\rm soc}^{p}}{2}\left(\frac{\cos^2\gamma}{\varepsilon_{\sigma}^{-}} + \frac{\sin^2\gamma}{\varepsilon_{\sigma}^{+}}\right)(c_A|1,-\tau\rangle^{A} + c_B|1,\tau\rangle^{B}) = \tau\alpha_I^{\sigma}(c_A|1,-\tau\rangle^{A} + c_B|1,\tau\rangle^{B}).
\end{aligned}$$

Similarly, the Bychkov-Rashba Hamiltonian can be expressed as the coupling of the p_z and s orbitals,

$$\hat{V}_{\rm BR} = \lambda_z\hat{\tilde{L}}\hat{\tilde{s}}\sum_{\alpha=A,B}|s^{\alpha}\rangle\langle p_z^{\alpha}| + \text{H.c.},$$

yielding a first order correction to the π orbitals of Eq. (3):

$$\left|\varphi_{\rm BR}^{(1)}\right\rangle = -i\lambda_z\tau c^{A}\hat{\tilde{L}}\hat{\tilde{s}}\left(\frac{\cos\gamma}{\varepsilon_{\sigma}^{+}}|\psi_{AB}^{+}\rangle - \frac{\sin\gamma}{\varepsilon_{\sigma}^{-}}|\psi_{AB}^{-}\rangle\right) - i\lambda_z\tau c^{B}\hat{\tilde{L}}\hat{\tilde{s}}\left(\frac{\cos\gamma}{\varepsilon_{\sigma}^{+}}|\psi_{BA}^{+}\rangle - \frac{\sin\gamma}{\varepsilon_{\sigma}^{-}}|\psi_{BA}^{-}\rangle\right).$$

Using $\hat{\tilde{L}}\hat{\tilde{s}} = (\hat{L}_{+}\hat{\sigma}_{-} + \hat{L}_{-}\hat{\sigma}_{+})/2 + \hat{L}_z\hat{s}_z$ and that $(\hat{L}_{+}\hat{\sigma}_{-} + \hat{L}_{-}\hat{\sigma}_{+})|1,\pm\tau\rangle^{\alpha} = \sqrt{2}\delta_{s_z,\mp\tau}|1,0\rangle^{\alpha} = \sqrt{2}\delta_{s_z,\mp\tau}|p_z^{\alpha}\rangle$, we obtain

$$\left|\varphi_{\rm BR}^{(1)}\right\rangle = -i\sqrt{2}\lambda_z s_z\cos\gamma\sin\gamma\left(\frac{1}{\varepsilon_{\sigma}^{+}} - \frac{1}{\varepsilon_{\sigma}^{-}}\right)(c_A|1,\tau\rangle^{B} + c_B|1,\tau\rangle^{A}) \simeq i\frac{2\lambda_z s_z}{3V_{sp\sigma}}(c_A|1,s_z\rangle^{B} + c_B|1,\tau\rangle^{A}),$$

where we can identify $\alpha_{\rm BR} = 2\lambda_z/3V_{sp\sigma}$. The derivation of $\alpha_{\rm BR}$ is similar, yielding $2\lambda_{\rm pia}/3V_{sp\sigma}$.

[1] P. A. M. Dirac, Proc. R. Soc. London A **117**, 610 (1928).
[2] W. Greiner, *Relativistic Quantum Mechanics* (Springer, Berlin, 1994).
[3] K. S. Novoselov, A. K. Geim, S. V. Morozov, D. Jiang, M. I. Katsnelson, I. V. Grigorieva, S. V. Dubonos, and A. A. Firsov, Nature (London) **438**, 197 (2005).
[4] M. I. Katsnelson, K. Novoselov, and A. K. Geim, Nat. Phys. **2**, 620 (2006).
[5] A. K. Geim and K. S. Novoselov, in *Nanoscience and Technology: A Collection of Reviews from Nature Journals* (World Scientific, Singapore, 2010), pp. 11–19.
[6] R. R. Nair, P. Blake, A. N. Grigorenko, K. S. Novoselov, T. J. Booth, T. Stauber, N. M. R. Peres, and A. K. Geim, Science **320**, 1308 (2008).
[7] M. Mecklenburg and B. C. Regan, Phys. Rev. Lett. **106**, 116803 (2011).
[8] A. Golub, R. Egger, C. Müller, and S. Villalba-Chávez, Phys. Rev. Lett. **124**, 110403 (2020).
[9] A. Giuliani, V. Mastropietro, and M. Porta, Ann. Phys. (NY) **327**, 461 (2012).
[10] C. L. Kane and E. J. Mele, Phys. Rev. Lett. **95**, 226801 (2005).
[11] C. L. Kane and E. J. Mele, Phys. Rev. Lett. **95**, 146802 (2005).
[12] J. Sichau, M. Prada, T. Anlauf, T. J. Lyon, B. Bosnjak, L. Tiemann, and R. H. Blick, Phys. Rev. Lett. **122**, 046403 (2019).
[13] J. Li *et al.*, arXiv:2103.15937.
[14] M. Prada, Phys. Rev. B **103**, 115425 (2021).

[15] J. A. Weil and J. R. Bolton, *Electron Paramagnetic Resonance: Elementary Theory and Practical Applications* (John Wiley & Sons, New York, 2006).
[16] C. Bloch, Nucl. Phys. **6**, 329 (1958).
[17] M. Mostafanejad, Int. J. Quantum Chem. **114**, 1495 (2014).
[18] C. Rudowicz, Magn. Reson. Rev. **13**, 1 (1987).
[19] C. P. Slichter, *Principles of Magnetic Resonance*, Springer Series in Solid-State Sciences, Vol. 1 (Springer, Berlin, 1990).
[20] A. H. Castro Neto, F. Guinea, N. M. R. Peres, K. S. Novoselov, and A. K. Geim, Rev. Mod. Phys. **81**, 109 (2009).
[21] M. I. Katsnelson, *Graphene: Carbon in Two Dimensions* (Cambridge University Press, Cambridge, 2012).
[22] U. R. Singh, M. Prada, V. Strenzke, B. Bosnjak, T. Schmirander, L. Tiemann, and R. H. Blick, Phys. Rev. B **102**, 245134 (2020).
[23] L. Banszerus, B. Frohn, T. Fabian, S. Somanchi, A. Epping, M. Müller, D. Neumaier, K. Watanabe, T. Taniguchi, F. Libisch, B. Beschoten, F. Hassler, and C. Stampfer, Phys. Rev. Lett. **124**, 177701 (2020).
[24] J. W. McClure and Y. Yafet, *Proceedings of the Fifth Conference on Carbon* (Pergamon, New York, 1962).
[25] S. Konschuh, *Spin-orbit Coupling Effects from Graphene to Graphite* (Universitätsbibliothek Regensburg, Regensburg, 2011).
[26] S. Konschuh, M. Gmitra, and J. Fabian, Phys. Rev. B **82**, 245412 (2010).
[27] D. Huertas-Hernando, F. Guinea, and A. Brataas, Phys. Rev. B **74**, 155426 (2006).
[28] R. Saito, G. Dresselhaus, and M. S. Dresselhaus, *Physical Properties of Carbon Nanotubes* (Imperial College Press, London, 1998).
[29] E. I. Rashba, Phys. Rev. B **79**, 161409(R) (2009).
[30] H. Min, J. E. Hill, N. A. Sinitsyn, B. R. Sahu, L. Kleinman, and A. H. MacDonald, Phys. Rev. B **74**, 165310 (2006).
[31] Y. Yao, F. Ye, X.-L. Qi, S.-C. Zhang, and Z. Fang, Phys. Rev. B **75**, 041401(R) (2007).
[32] M. Gmitra, D. Kochan, and J. Fabian, Phys. Rev. Lett. **110**, 246602 (2013).
[33] D. Kochan, S. Irmer, and J. Fabian, Phys. Rev. B **95**, 165415 (2017).
[34] J. P. Robinson, H. Schomerus, L. Oroszlány, and V. I. Fal'ko, Phys. Rev. Lett. **101**, 196803 (2008).
[35] C.-C. Liu, H. Jiang, and Y. Yao, Phys. Rev. B **84**, 195430 (2011).
[36] T. J. Lyon, J. Sichau, A. Dorn, A. Zurutuza, A. Pesquera, A. Centeno, and R. H. Blick, Appl. Phys. Lett. **110**, 113502 (2017).
[37] T. J. Lyon, J. Sichau, A. Dorn, A. Centeno, A. Pesquera, A. Zurutuza, and R. H. Blick, Phys. Rev. Lett. **119**, 066802 (2017).
[38] R. G. Mani, J. Hankinson, C. Berger, and W. A. De Heer, Nat. Commun. **3**, 996 (2012).
[39] Z. Wilamowski, H. Malissa, F. Schäffler, and W. Jantsch, Phys. Rev. Lett. **98**, 187203 (2007).
[40] J. Serrano, M. Cardona, and T. Ruf, Solid State Commun. **113**, 411 (2000).
[41] F. Hermann and S. Skillman, *Atomic Structure Calculations* (Prentice-Hall, Englewood Cliffs, NJ, 1963).
[42] http://www.nanomeas.com